Optics Letters

Demonstration of a highly efficient terahertz flat lens employing tri-layer metasurfaces

Chun-Chieh Chang,[1,†] Daniel Headland,[2,†] Derek Abbott,[2] Withawat Withayachumnankul,[2] and Hou-Tong Chen[1,*]

[1]Center for Integrated Nanotechnologies, Los Alamos National Laboratory, Los Alamos, New Mexico 87545, USA
[2]School of Electrical and Electronic Engineering, The University of Adelaide, Adelaide, SA 5005, Australia
*Corresponding author: chenht@lanl.gov

Received 30 January 2017; revised 5 April 2017; accepted 11 April 2017; posted 12 April 2017 (Doc. ID 285767); published 1 May 2017

We demonstrate a terahertz flat lens based on tri-layer metasurfaces allowing for broadband linear polarization conversion, where the phase can be tuned through a full 2π range by tailoring the geometry of the subwavelength resonators. The lens functionality is realized by arranging these resonators to create a parabolic spatial phase profile. The fabricated 124-μm-thick device is characterized by scanning the beam profile and cross section, showing diffraction-limited focusing and ~68% overall efficiency at the operating frequency of 400 GHz. This device has potential for applications in terahertz imaging and communications, as well as beam control in general.

OCIS codes: (230.0230) Optical devices; (230.4000) Microstructure fabrication; (160.3918) Metamaterials; (050.1965) Diffractive lenses; (110.6795) Terahertz imaging.

https://doi.org/10.1364/OL.42.001867

Particular constraints in the terahertz range—namely, historical difficulties in generating power [1], high atmospheric attenuation [2], and free-space path loss—result in a pronounced need for beam control devices in order to minimize power projected in unwanted directions [3]. Conventional geometric lenses and reflector devices are mature and readily available in the terahertz range, but their physical thickness and weight pose disadvantages. Compact, flat-profile beam control devices of subwavelength thickness are generally preferable for practical applications. A promising approach to realizing such devices is the use of metasurfaces [4–7] consisting of a planar array of heterogeneous elements that individually impart some particular phase shift to incident waves [8,9]. The aggregation of these phases produces a wavefront that dictates the form of the ensuing propagating beam, and desirable behaviors have previously been demonstrated in transmission [10] or reflection [11–14] in the terahertz range. A full 2π phase tunability range is required for optimal wavefront engineering, and in transmission this typically necessitates the use of multiple layers of metallic resonators [15–17], as a single layer is insufficient to support magnetic resonance [18]. An alternative approach is to make use of the transmitted cross-polarization by employing anisotropic resonators [8], where the phase can be tuned by tailoring the resonator geometry, realizing functionality such as optical beam focusing [19,20].

In the terahertz range, single-layer metasurface flat lenses have been demonstrated using C-shaped [21,22] and complementary V-shaped resonators [23–26], which offer cross-polarized transmission efficiency below 25%, and in experiments the focusing efficiency was only a few percent. In previous work, the cross-polarization conversion efficiency was greatly enhanced by making use of additional nonresonant layers, and the tunable phase was exploited to enable a beam-steering device, with an experimentally demonstrated peak efficiency of 50%–60% over a broad frequency range around 1.2 THz [27]. In the present work, we adapt this approach to create a highly efficient flat lens operating at around 400 GHz. The demonstrated flat lens is of practical value, as it can be employed to enhance antenna gain for high-volume communications [28] and focus radiation for imaging applications [29]. Additionally, the selection of an operating frequency toward the lower end of the terahertz range, as opposed to more terahertz-representative values such as 1 THz, is informed by lower absorption due to atmospheric gases [2], as well as a greater degree of compatibility with compact electronic terahertz sources and detectors [30,31]. In principle, however, a metasurface of this sort can straightforwardly be scaled in size to serve higher frequencies, if desired.

Figure 1(a) illustrates a unit cell of the metasurface, consisting of three layers of subwavelength metallic structures—two orthogonal wire grids and an array of anisotropic resonators in between. When the middle resonator is excited by the incident radiation polarized in the x direction, the resultant electric dipole has a component that is orthogonal to the incident polarization, i.e., in the y direction, and consequently, it radiates waves in the cross-polarization. Alternatively, we can understand that the anisotropic resonator is birefringent, converting the incident linear polarization to elliptical polarization and creating the cross-polarization component. The use of two nonresonant wire grids forms a cavity to dramatically improve the efficiency of the polarization conversion. Essentially, the front wire grid allows the incident waves to transmit through and interact with the resonator, and at the same time blocks the

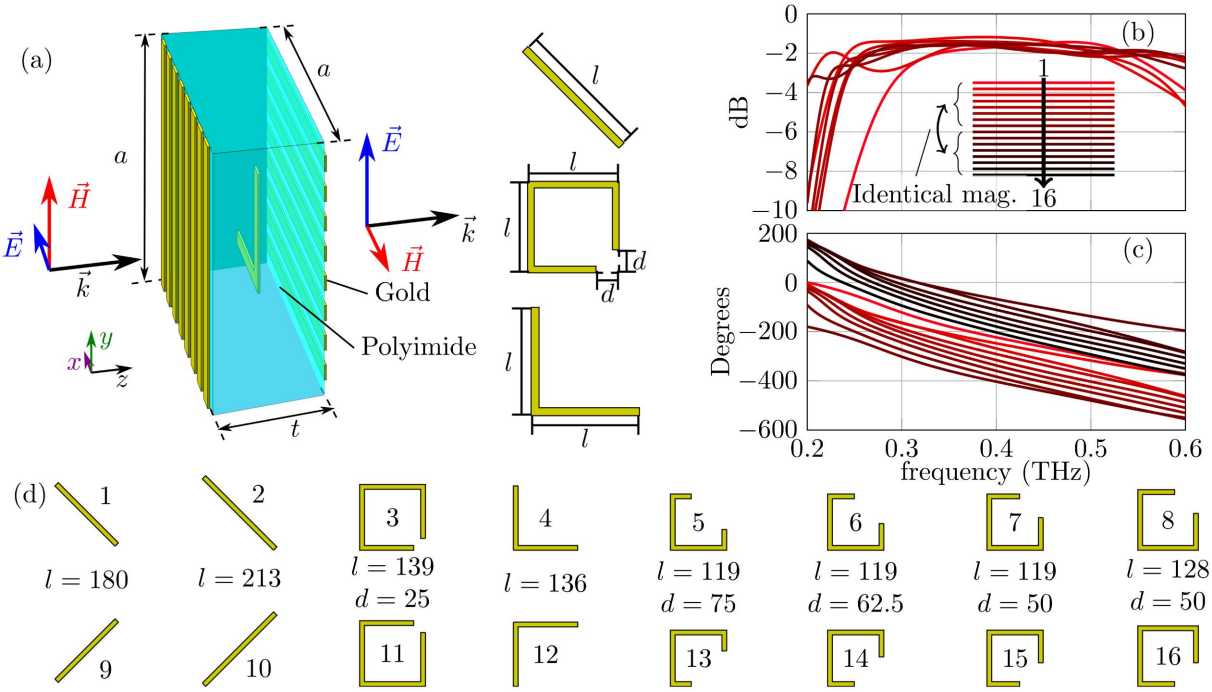

Fig. 1. (a) Unit cell structure of the tri-layer metasurface that allows for broadband linear polarization conversion, where $a = 160$ μm and $t = 120$ μm. The diagrams on the right show three different classes of resonator shapes used in this work. There are 2-μm-thick polyimide cap layers at the input and output surfaces, which are omitted for clarity. (b) Magnitude and (c) phase response of the cross-polarized transmission for the 16 resonator structures shown in (d). Note that resonators 9–16 formed by flipping resonators 1–8 over the x axis. Consequently, their magnitude responses correspond identically, and are omitted from (b). The track width of all metal microstructures is 10 μm, and the unit for the specified dimensions in (d) is μm.

backpropagating waves with cross-polarization generated from the resonator. The back wire grid reflects the copolarized waves back to the resonator for additional interactions, but allows the transmission of the cross-polarization. This enhances the conversion to cross-polarization in the forward direction, and ultimately there is only cross-polarized transmission (desirable) and copolarized reflection (undesirable). The latter can be minimized by appropriately tuning the dielectric spacer thickness, which leads to destructive interference of multireflection from the metasurface cavity [32].

In principle, any anisotropic resonators can be applied in such tri-layer metasurfaces to achieve linear polarization conversion. It has been shown that varying the resonator geometry can result in different transmission phases [27]. In this work we use three different basic resonator forms, as shown in Fig. 1(a). The unit cell response is investigated with full-wave simulations using CST Microwave Studio, representing an infinite, uniform array of elements that is excited with normally incident radiation. The obtained cross-polarized transmission magnitude and phase are plotted in Figs. 1(b) and 1(c), respectively, for a total of 16 different resonators, shown in Fig. 1(d). It can be seen from the results in Fig. 1(b) that the transmission efficiency at the nominal operating frequency of 400 GHz ranges from 68% to 76%, and it has at least 50% efficiency over a 250 GHz range that spans 300 to 550 GHz, equivalent to 62.5% fractional bandwidth. More important, the phase response results in Fig. 1(c) show a smooth, near-linear phase gradient for all resonators, with an approximate phase step of $\pi/8$ separating adjacent phase responses across the entire usable frequency range. Note that resonators 9–16 are obtained by simply flipping resonators 1–8 in the x axis, which alters their phase response by 180°, but with identical transmission magnitudes between corresponding resonators, as evidenced in Figs. 1(b) and 1(c).

In order to function as a lens, the metasurface must impart the following phase distribution onto the transmitted radiation [19]:

$$\phi(r) = k_0\left(\sqrt{F^2 + r^2} - F\right), \tag{1}$$

where k_0 is the free-space wavenumber, F is the desired focal length, and r is the distance from the center of the flat lens. It is noted that the engineering phase convention is used, in which a less-positive phase corresponds to a greater phase delay. This phase distribution can be mapped to the 16 resonator designs via their discrete phase responses. For this design, a focal length of 50 mm at the nominal operating frequency of 400 GHz is selected, and the results of this procedure are given in Fig. 2(a).

The fabrication of the metasurface flat lens begins by spin coating and thermal curing a 2-μm-thick polyimide layer (HD MicroSystems PI-2525) onto a 4 in (~100 mm). Si substrate. A 200-nm-thick gold (Au) back grating (track width = 10 μm; duty cycle = 50%) is then fabricated using conventional contact lithography, electron-beam evaporation, and metal lift-off. A 60-μm-thick polyimide layer is subsequently spin coated and thermally cured on hotplates at 300°C for 150 min, with a temperature ramp of 2.5°C/min. The resonator array containing 16 different classes of Au resonator is fabricated atop this polyimide layer, following the same steps used to realize the Au back grating. A second 60-μm-thick polyimide layer is then spin coated and thermally cured on top of the resonator layer,

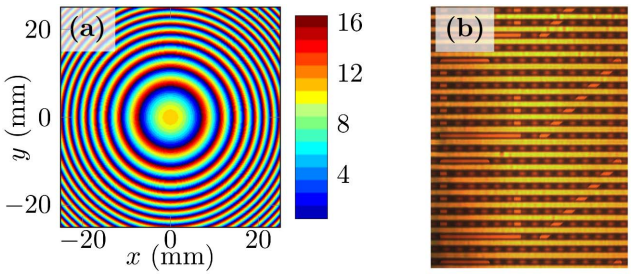

Fig. 2. (a) Spatial phase profile of the metasurface enabling lens function, where the color coding represents the use of the different resonators listed in Fig. 1(d), spanning a full 2π phase range; (b) a micrograph of a portion of the fabricated sample, showing two classes of resonators.

followed by the fabrication of the Au front grating, which is oriented orthogonally to the Au back grating. Another 2-μm-thick polyimide cap layer is subsequently deposited and thermally cured in order to encapsulate the entire structure. Finally, the fabricated structure is mechanically peeled off from the Si substrate in order to establish a freestanding sample. A micrograph of a portion of the resulting sample is given in Fig. 2(b), showing well-defined resonators and wire grids. The total area of the sample is ∼50 mm × 50 mm, and hence there are a total of ∼98,000 individual resonator elements.

The sample is excited with a collimated beam of the appropriate polarization. The central portion of the incident beam is approximated by a Gaussian beam with a radius of 12 mm at the operating frequency, but it also exhibits some intrinsic frequency-dependent irregularities. The cross section (xy) and profile (xz) of the focused beam are raster scanned; the results are presented in Fig. 3. Scans are presented at three frequencies of interest, namely, 350 GHz, the designed operating frequency of 400 GHz, and 450 GHz. It is noted that the z axis is defined relative to the focal plane at 400 GHz, rather than the flat lens device itself, as the realized focal distance is not explicitly known due to factors including divergence of the incident beam, as well as the internal configuration of the detector photoconductive antenna (PCA). It is apparent from the xy scan that a focal spot is produced, shown in Fig. 3(c) at the operating frequency, and this validates the functionality of the nonuniform metasurface. The central portion of this focal spot is closely approximated by a narrow Gaussian beam, albeit with some undesired fields surrounding the focus. These fields are associated with irregularities in the incident beam, which causes the output phase distribution to deviate from those specified by Eq. (1). The beam diameter of the central portion is determined by curve fitting to be 2.3 mm, but it is worth noting that this is spread by the detector, which is approximated as a Gaussian aperture with a diameter of 1.32 mm. As such, the true beam diameter is determined to be ∼1.88 mm, which is close to the diffraction-limited value of ∼1.98 mm based on the input beam radius of 12 mm. From the xz scan at the operating frequency presented in Fig. 3(d), the progression of the beam is revealed, and it can be seen that the beam passes through its focus as expected. However, the aforementioned irregularities of the incident beam are also evident here, as the beam does not exhibit a strictly Gaussian intensity profile. For instance, there are submaxima at either side of the optical axis after it passes through its focus, which appear to correspond to the aforementioned undesired fields surrounding the focus in the xy scans in Fig. 3(c).

A flat lens of this sort is expected to be dispersive, given the approximately proportional relationship between the focal length and frequency for the frequency-invariant relative phase distribution. This is especially true given the near-constant difference in phase between resonator elements across the usable frequency range shown in Fig. 1(c). For this particular flat lens, this dispersion relation predicts a difference of ∼6.25 mm in the focal length for a 50 GHz difference in frequency. As such, the xy scans shown in Figs. 3(a) and 3(e) are not at the device's focal plane, resulting in a broader spread in the electric field distribution. It is also worth noting that the scan in Fig. 3(a) shows an annular-like field distribution, which is ascribed to irregularities in the incident beam. The calculated focal plane positions for 350 and 400 GHz are consistent with the xz scans given in Figs. 3(b) and 3(d). However, the distance is greater for the scan shown in Fig. 3(f). We attribute this to the frequency-dependent divergence of the incident beam, which exaggerates the spatial dispersion of the metasurface.

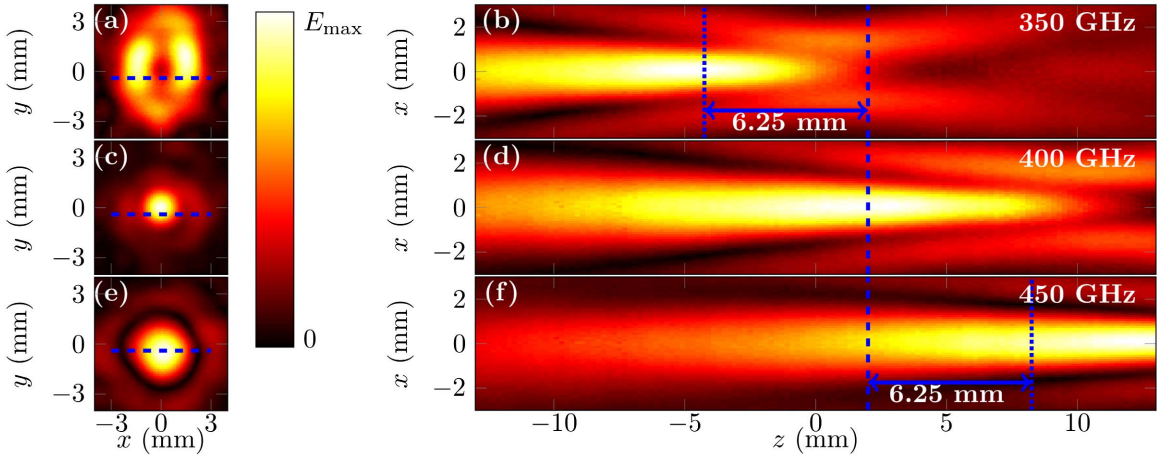

Fig. 3. Measured raster-scanned field distributions spanning a 100 GHz range around the nominal 400 GHz operating frequency. (a, c, e) xy-plane cross sections of the focused beam at 350, 400, and 450 GHz, respectively; (b, d, f) xz-plane beam profiles for the corresponding frequencies. Blue dashed lines give the intersections between the xy and xz planes in each of the plots, and blue dotted lines give the expected locations of the focal spots based on a simplified dispersion model. All field plots are normalized to their respective maxima, in linear scale.

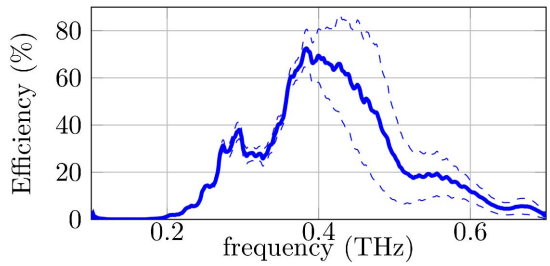

Fig. 4. Overall efficiency, investigated by single-pixel measurements, with error bars at one standard deviation given as dashed lines.

Of key interest to the performance of this device is the overall efficiency, and hence we evaluate this experimentally. The approach that we have employed is to compare the peak power delivered to the focal spot at 400 GHz with the power delivered by a standard polymethylpentene lens of the same focal length serving as a reference. Discrepancies in output polarization and device aperture are compensated by setting the detector at a 45° angle and passing the incident beam through an iris with an ∼25 mm diameter, ensuring identical coverage of the incident terahertz beam. The dissipation and reflection losses of the reference lens are compensated analytically, based on material properties from the literature [33], and this measurement procedure is repeated five times in order to evaluate the associated degree of uncertainty. The results are presented in Fig. 4, revealing a mean peak efficiency of ∼68% at the nominal operating frequency of 400 GHz, which is consistent with the unit cell simulations. Additionally, we extract a −3 dB spectral bandwidth of 150 GHz from these results, spanning from 340 to 490 GHz. It is also worth noting that the standard error increases markedly above the operating frequency, which is likely due to a diminishing dynamic range with the increase in frequency.

In summary, we have presented the design, fabrication, and characterization of a terahertz metasurface flat lens operating in the vicinity of 400 GHz. The demonstrated diffraction-limited focusing capability and operating frequency are amenable to practical applications including imaging and high-volume communications. The bandwidth of this device is mainly limited by spatial dispersion, and is found to be approximately 37%, which corresponds to 150 GHz of absolute spectral bandwidth. The transmission efficiency of the metasurface is experimentally evaluated to be ∼68% at the operating frequency.

Funding. Australian Research Council (ARC) (DP140104651, FT120100351); Los Alamos National Laboratory (LANL); U.S. Department of Energy (DOE) (DE-AC52-06NA25396).

Acknowledgment. D. A. would like to thank the ARC for providing funding. The authors gratefully acknowledge John Nogan and Willard Ross for valuable discussion and assistance in device fabrication. This work was performed, in part, at the Center for Integrated Nanotechnologies, a U.S. Department of Energy Office of Basic Energy Sciences Nanoscale Science Research Center operated jointly by Los Alamos and Sandia National Laboratories. LANL, an affirmative action/equal opportunity employer, is operated by Los Alamos National Security, LLC, for the National Nuclear Security Administration of the U.S. Department of Energy.

[†]These authors contributed equally to this work.

REFERENCES

1. J. Chamberlain, Philos. Trans. R. Soc. London A **362**, 199 (2004).
2. ITU-R 676-10, "Attenuation by atmospheric gases," (2013).
3. H.-J. Song and T. Nagatsuma, IEEE Trans. Terahertz Sci. Technol. **1**, 256 (2011).
4. H.-T. Chen, A. J. Taylor, and N. Yu, Rep. Prog. Phys. **79**, 076401 (2016).
5. S. B. Glybovski, S. A. Tretyakov, P. A. Belov, Y. S. Kivshar, and C. R. Simovski, Phys. Rep. **634**, 1 (2016).
6. N. Yu and F. Capasso, Nat. Mater. **13**, 139 (2014).
7. A. V. Kildishev, A. Boltasseva, and V. M. Shalaev, Science **339**, 1232009 (2013).
8. N. Yu, P. Genevet, M. A. Kats, F. Aieta, J.-P. Tetienne, F. Capasso, and Z. Gaburro, Science **334**, 333 (2011).
9. S. Sun, Q. He, S. Xiao, Q. Xu, X. Li, and L. Zhou, Nat. Mater. **11**, 426 (2012).
10. S.-G. Park, K. Lee, D. Han, J. Ahn, and K.-H. Jeong, Appl. Phys. Lett. **105**, 091101 (2014).
11. T. Niu, W. Withayachumnankul, B. S.-Y. Ung, H. Menekse, M. Bhaskaran, S. Sriram, and C. Fumeaux, Opt. Express **21**, 2875 (2013).
12. T. Niu, W. Withayachumnankul, A. Upadhyay, P. Gutruf, D. Abbott, M. Bhaskaran, S. Sriram, and C. Fumeaux, Opt. Express **22**, 16148 (2014).
13. T. Niu, A. Upadhyay, W. Withayachumnankul, D. Headland, D. Abbott, M. Bhaskaran, S. Sriram, and C. Fumeaux, Appl. Phys. Lett. **107**, 031111 (2015).
14. D. Headland, E. Carrasco, S. Nirantar, W. Withayachumnankul, P. Gutruf, J. Schwarz, D. Abbott, M. Bhaskaran, S. Sriram, J. Perruisseau-Carrier, and C. Fumeaux, ACS Photon. **3**, 1019 (2016).
15. C. G. Ryan, M. R. Chaharmir, J. Shaker, J. R. Bray, Y. M. Antar, and A. Ittipiboon, IEEE Trans. Antennas Propag. **58**, 1486 (2010).
16. C. Pfeiffer and A. Grbic, IEEE Trans. Microwave Theory Tech. **61**, 4407 (2013).
17. L.-W. Chen, Y. Ge, and T. S. Bird, Electron. Lett. **52**, 1653 (2016).
18. F. Monticone, N. M. Estakhri, and A. Alù, Phys. Rev. Lett. **110**, 203903 (2013).
19. F. Aieta, P. Genevet, M. A. Kats, N. Yu, R. Blanchard, Z. Gaburro, and F. Capasso, Nano Lett. **12**, 4932 (2012).
20. X. Ni, S. Ishii, A. V. Kildishev, and V. M. Shalaev, Light Sci. Appl. **2**, e72 (2013).
21. X. Zhang, Z. Tian, W. Yue, J. Gu, S. Zhang, J. Han, and W. Zhang, Adv. Mater. **25**, 4567 (2013).
22. Q. Wang, X. Zhang, Y. Xu, Z. Tian, J. Gu, W. Yue, S. Zhang, J. Han, and W. Zhang, Adv. Opt. Mater. **3**, 779 (2015).
23. D. Hu, X. Wang, S. Feng, J. Ye, W. Sun, Q. Kan, P. J. Klar, and Y. Zhang, Adv. Opt. Mater. **1**, 186 (2013).
24. X.-Y. Jiang, J.-S. Ye, J.-W. He, X.-K. Wang, D. Hu, S.-F. Feng, Q. Kan, and Y. Zhang, Opt. Express **21**, 30030 (2013).
25. J. He, X. Wang, D. Hu, J. Ye, S. Feng, Q. Kan, and Y. Zhang, Opt. Express **21**, 20230 (2013).
26. D. Hu, G. Moreno, X. Wang, J. He, A. Chahadih, Z. Xie, B. Wang, T. Akalin, and Y. Zhang, Opt. Commun. **322**, 164 (2014).
27. N. K. Grady, J. E. Heyes, D. R. Chowdhury, Y. Zeng, M. T. Reiten, A. K. Azad, A. J. Taylor, D. A. Dalvit, and H.-T. Chen, Science **340**, 1304 (2013).
28. X. Yu, R. Asif, M. Piels, D. Zibar, M. Galili, T. Morioka, P. U. Jepsen, and L. K. Oxenløwe, IEEE Trans. Terahertz Sci. Technol. **6**, 765 (2016).
29. E. Ojefors, U. R. Pfeiffer, A. Lisauskas, and H. G. Roskos, IEEE J. Solid-State Circuits **44**, 1968 (2009).
30. U. R. Pfeiffer, Y. Zhao, J. Grzyb, R. Al Hadi, N. Sarmah, W. Förster, H. Rücker, and B. Heinemann, IEEE J. Solid-State Circuits **49**, 2938 (2014).
31. J. Grzyb, B. Heinemann, and U. R. Pfeiffer, IEEE J. Solid-State Circuits **51**, 3063 (2016).
32. H.-T. Chen, Opt. Express **20**, 7165 (2012).
33. A. Podzorov and G. Gallot, Appl. Opt. **47**, 3254 (2008).